

1 **Multitemporal UAV LiDAR detects seasonal heave and**
2 **subsidence on palsas**

3 Cas Renette¹, Mats Olvmo¹, Sofia Thorsson¹, Björn Holmer¹, Heather Reese¹

4 ¹Department of Earth Sciences, University of Gothenburg, Gothenburg, Sweden

5 *Correspondence to:* Cas Renette (cas.renette@gvc.gu.se)

6

7 **Abstract**

8 In the context of the accelerating impacts of climate change on permafrost landscapes, we use an uncrewed
9 aerial vehicle (UAV) carrying a LiDAR scanner to investigate seasonal terrain changes in palsas – mounds
10 of frozen peat – since other remote sensing methods have struggled to capture the full dynamics of these
11 landforms. We investigated two palsas (4–5 m in height) in Sweden's largest palsa mire complex, where
12 we performed five field campaigns between September 2022 and September 2023 to track intra-annual
13 frost heave and thaw subsidence. Our approach allowed us to create digital terrain models (DTMs) from
14 high density point clouds (>1,000 points/m²) and analyze elevation changes over time. We found that both
15 palsas heaved on average 0.15 m (and up to 0.30 m) from September to April and subsided back to their
16 height from the previous year, or slightly below, over the course of the following summer. At one of the
17 palsas, we observed a notable lateral degradation hotspot over the study period in a 225 m² area, with 0.5–
18 1.9 m height loss, likely initiated during the preceding warm and wet summer months. Part of this
19 degradation occurred between September 2022 and April 2023, suggesting that the degradation of these
20 palsas is not limited to the summer months. Our study shows the substantial value of using UAV LiDAR for
21 understanding how permafrost areas are changing. It facilitates tracking the ongoing effects of climate
22 change and highlights palsa dynamics that would not be captured by annual measurements alone.

23

24 1 Introduction

25 In the face of accelerating climate change, permafrost – defined as ground that remains at or below 0 °C
26 for at least two consecutive years (Harris et al., 1988) – is warming at a global scale (Biskaborn et al.,
27 2019). Permafrost regions hold approximately 50% (1300±200 Pg) of the world's terrestrial carbon, making
28 them vital to the global climate system (Hugelius et al., 2020). A significant amount (415±150 Pg carbon)
29 is stored in northern peatlands, nearly half of which is affected by permafrost (Hugelius et al., 2020). In the
30 discontinuous and sporadic permafrost zones, peatland permafrost can be found in palsa mires, consisting
31 of peat plateaus and palsas. Palsas are peat mounds with a core of perennially frozen soil (Seppälä, 1986).
32 Palsa mires are a sensitive and heterogeneous ecosystem, which are vulnerable to increased air
33 temperatures and precipitation in the Arctic (Luoto et al., 2004a).

34 The climatic space for palsas, typically with a mean annual air temperature between -3 °C and -5 °C and
35 mean annual precipitation <450 mm, according to Luoto et al. (2004a), is projected to disappear in
36 Fennoscandia by the end of the 21st century (Fewster et al., 2022). In recent studies, an increasing lateral
37 degradation rate of palsas is reported (Borge et al., 2017; Mamet et al., 2017; Olvmo et al., 2020) which
38 may have far-reaching consequences for these ecosystems and biodiversity of the subarctic region (Luoto
39 et al., 2004b; Swindles et al., 2015). For example, the loss of palsas can lead to the decline of specialized
40 plant species that are adapted to the unique, dry conditions of palsas. Additionally, animals that depend on
41 these habitats, such as certain bird species and small mammals are affected (Luoto et al., 2004b). In
42 addition to the threat to biodiversity, the degradation of palsas also impacts reindeer herding, berry picking
43 and transport for local communities, as these elevated, often dry, parts of the landscape shrink and become
44 more fragmented. The transition from a palsa to a lower lying, wet fen, is also associated with an increase
45 in CH₄ and CO₂ emissions (e.g. Łakomiec et al., 2021; Pirk et al., 2024; Swindles et al., 2015; Voigt et al.,
46 2019) as the stored carbon in these peatlands is subject to microbial re-mobilization when permafrost
47 thaws. The climatic feedback mechanism further highlights the need for continued monitoring of these
48 environments. Therefore, palsa mires are a priority habitat of the EU Species and Habitat Directive (*EUNIS*
49 *-Factsheet for Palsa Mires*, 2013). However, in Sweden only about half (47%) of the total palsa area is
50 situated within a protected area (Backe, 2014).

51 The degradation of permafrost in palsas is indicated by both lateral erosion and vertical subsidence. Lateral
52 erosion refers to the horizontal shrinkage of the permafrost body along the edges of palsas, often resulting
53 in the formation or expansion of connected water bodies, i.e. thermokarst lakes (Martin et al., 2021). Vertical
54 subsidence, on the other hand, involves the downward sinking of the ground surface as a result of the
55 melting of excess ground ice, leading to a drop in surface elevation. In addition to this, the elevation of
56 permafrost terrain fluctuates cyclically due to annual freeze-thaw cycles within the active layer (Gruber,
57 2020; Iwahana et al., 2021), although this has not been explicitly studied on palsas. During fall, freezing of
58 water in the soil and its expansion, in addition to the formation of seasonally segregated ice, can cause
59 heaving of the terrain, while terrain subsidence, caused by the melting of both pore ice and segregated ice,
60 occurs during spring and summer (Fu et al., 2022). The melting of excess ground ice (i.e. ice that is in
61 excess of the total pore volume of the ground in unfrozen conditions; Harris et al., 1988) below the active
62 layer causes longer-term subsidence as result of permafrost thaw. Therefore, thaw-subsidence rates are
63 generally higher in ice-rich than in ice-poor permafrost soils (Gruber, 2020; Zwieback & Meyer, 2021).

64 While there is growing awareness of the importance of monitoring palsa mires, there is a lack of quantitative
65 measurements of their intra-annual heave and subsidence patterns. de la Barreda-Bautista et al. (2022)
66 used InSAR data to analyze thaw-season subsidence on palsas in northern Sweden, finding only sub-cm
67 scale surface level changes. They suggest that this method likely highly underestimated actual
68 displacement rates as a result of spatial averaging. In other recent studies with attempts to quantify both
69 lateral and vertical changes in palsas or peat plateaus, the focus was on multi-year timescales (e.g. Martin
70 et al., 2021; Verdonen et al., 2023) and not on changes occurring within a year. UAV photogrammetry to
71 create digital surface models (DSMs) to study palsas and peat plateaus has been applied more frequently
72 in recent years (e.g., de la Barreda-Bautista et al., 2022; Krutskikh et al., 2023; Martin et al., 2021; Verdonen
73 et al., 2023). However, as described in Verdonen et al. (2023), change analysis from DSMs created with
74 UAV photogrammetry is sensitive to relatively minor changes in vegetation and light conditions. Advances
75 in uncrewed aerial vehicles (UAV or drone) in combination with light detection and ranging (LiDAR)
76 technology (Ostrowski et al., 2017) have made it possible to collect accurate, high-resolution (cm-scale)
77 digital terrain models (DTMs) and DSMs. LiDAR sensors can prove advantageous over regular
78 photographic Red-Green-Blue (RGB) imagery, in that LiDAR can penetrate through small gaps in the

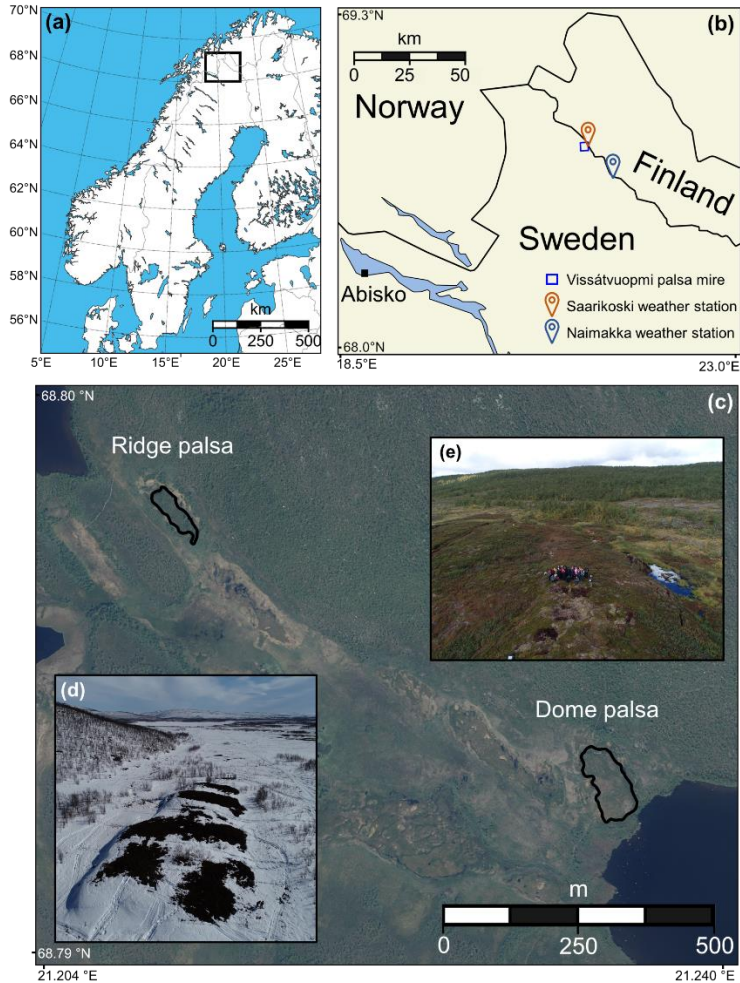
79 vegetation allowing creation of DTMs of the underlying ground, whereas terrain elevation models from RGB
80 cameras require clear sight to the ground surface. LiDAR can also be used in low-light conditions as
81 opposed to RGB imagery, which can be beneficial in the Arctic, where daylight is limited during parts of the
82 year. Another advantage that UAV LiDAR data holds is the absence of need of ground control points (GCPs)
83 due to the potentially low bias of UAV LiDAR data positional errors. This advantage drastically saves time
84 and thus costs on repeated visits (Harder et al., 2020). Therefore, the use of repeat UAV LiDAR scanning
85 is a promising tool for accurate change detection (Curcio et al., 2022; Harder et al., 2020; Jacobs et al.,
86 2021; Lin et al., 2019), but has not yet been widely used to monitor permafrost features. In this study, our
87 objective is to detect and quantify the intra-annual vertical heave and subsidence of two palsas using repeat
88 measurements from UAV LiDAR data.

89 **2 Study site: Vissátvuopmi palsa complex**

90 Located near the Finnish border, and just southwest of the Könkämäeno river, Vissátvuopmi is the largest
91 of the in total eight named coherent palsa mire complexes in Sweden (ca. 150 ha of palsa area; Backe,
92 2014) at N 68°47'50", E 21°11'30" (Fig. 1). According to InSAR data from 2017, 55% of the total area of
93 these eight palsa complexes is subsiding, compared to 98% of the Vissátvuopmi area (Valman et al., 2024).
94 Though notably, only Vissátvuopmi and Árbuvuopmi (northwest of Vissátvuopmi) are not part of the EU
95 Natura 2000 network.

96 Surrounded by mountains up to 700 m a.s.l., the valley in which Vissátvuopmi is located has several larger
97 lakes, thermokarst features and fens. Two distinct palsas, one ridge-shaped and one dome-shaped (called
98 the "Ridge" and "Dome" palsas from hereon) situated at the foot-slope of a bedrock hill, are the focus of
99 this study and are located between 443 and 452 m a.s.l. (Fig. 1c). Water tables typically do not rise above
100 the mire surface in most of the surroundings of the two studied palsas, except for thermokarst ponds that
101 border the palsas. In September 2023, the Dome palsa was approximately 170 meters in length and 75
102 meters in width, with an area of 11408 m² and its highest point about 4 meters above the surrounding mire.
103 The Ridge palsa measures about 125 meters in length and 40 meters in width, with an area of 3522 m² and
104 its highest point being roughly 5 meters above the adjacent mire terrain. The Dome palsa is taller on its
105 northern and eastern sides, while it flattens out on the western and southern sides. An all-terrain vehicle

106 (ATV) track runs over the northeastern part of the palsa, which most certainly contributes to amplified
 107 degradation of the underlying permafrost by collecting snow and water. The track is visible in aerial photos
 108 from 1994 but is absent in the 1963 photos. A natural depression in the center part of the palsa has the
 109 same effect and further fragments this palsa. The Ridge palsa is smaller in area but slightly taller. This
 110 palsa consists of several crests of similar elevation with depressions in between. The southeastern margin
 111 of this palsa is 'tail-shaped' and of lower elevation.

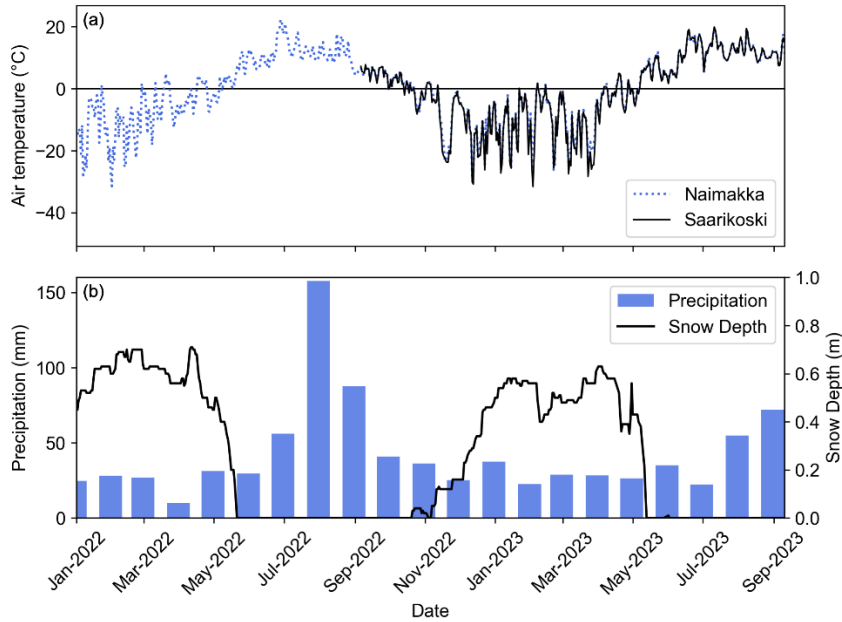


112
 113 **Figure 1. (a,b) Location of the Vissátvuopmi palsa mire complex and used weather stations in Northern**
 114 **Sweden. (c) Orthophoto from 2021 (© Lantmäteriet, 2021) showing a segment of the palsa mire and the location**
 115 **of the two studied palsas. (d) Oblique UAV image highlighting the partly snow-covered Ridge palsa in April**
 116 **2023. (e) Oblique UAV image of the Dome palsa in September 2023.**

117 The vegetation over the palsa mire complex is characterized by a mosaic of marshes with grasses and
 118 sphagnum mosses, wet heaths with willow, and drier areas with subalpine shrub heath. Birch forest occurs

119 primarily on the slopes surrounding the mire, however, birches are also growing within the palsa mire
120 complex. The palsa vegetation consists of dry heath and mesic heath (Andersson et al., 1985) where the
121 field layer is predominantly low-growing *Betula nana* (< 35 cm in mean height), *Empetrum nigrum* ssp
122 *hermaphroditum* and *Rubus chamaemorus*. The bottom layer consists of lichens in higher and drier areas
123 of the palsa, while sphagnum mosses are in lower-lying, wetter areas. At the edges of the palsa, particularly
124 where pools of water have formed, grasses such as *Carex rotundata* and *C. saxatilis* are common, in
125 addition to *Eriophorum russeolum* (Backe, 2014). The Ridge palsa has a few birch trees growing on the
126 north and south parts of the palsa.

127 The Köppen climate type is Subarctic (Dfc) and a weather station operated by the Swedish Meteorological
128 Institute (SMHI) in Naimakka (established in 1944), ca. 18 km east of the study site observed a mean annual
129 air temperature of of -1.5 °C and mean annual precipitation was 460 mm in the 1991–2020 standard period.
130 In September 2022, a HOBO® U30-NRC (Onset Computer Corporation) weather station was set up in the
131 nearby settlement of Saarikoski, ca. 1.5 km from the study site (see Fig. 1b for location of the two weather
132 stations). At this station, air temperatures at 2 m above the ground surface are recorded at two-hour
133 intervals. Both precipitation and snow depth have been monitored by SMHI since 2015 at Saarikoski. It is
134 notable that in July 2022 the monthly precipitation was 158 mm, which is more than one-third of the mean
135 annual precipitation (Fig. 2).



136

137 **Figure 2. Weather data in the study region between January 2022 and September 2023. (a) Mean daily air**
 138 **temperature at ca. 1.5 km (Saarikoski) and at ca. 18 km (Naimakka) from the studied palsas. (b) Monthly**
 139 **precipitation and snow depth observed at Saarikoski.**

140 Based on aerial photo interpretation, Olvmo et al. (2020) reported average areal decay rates of $-0.71\%a^{-1}$
 141 and $-1.25\%a^{-1}$ in the Dome and Ridge palsa respectively between 1955 and 2016. Additionally, they
 142 concluded that palsas in the Vissátvuopmi complex have most likely been in a phase of degradation since
 143 the early 20th century.

144 **3 Data and Methods**

145 **3.1 LiDAR data acquisition**

146 We used repeat UAV-borne LiDAR scanning to obtain point clouds and create raster-based DTMs at a high
 147 temporal and spatial resolution. Flights were performed on 4 September 2022, 26 April 2023, 18 June 2023,
 148 19 July 2023, and 7 September 2023. We conducted the scans on these dates to capture the state of the
 149 palsas at the end of summer, then observed them when frozen, and continued tracking them throughout
 150 the proceeding thawing season. A DJI Matrice 300 RTK UAV was equipped with a YellowScan Mapper
 151 (YSM) LiDAR scanner in September 2022 and a YellowScan Mapper + (YSM+) in all following flights (Fig.

152 3). These are lightweight Livox LiDAR scanners with an Applanix GNSS/INS system. Table 1 shows the
 153 properties of the flights and scanner(s). The vertical accuracy and precision of these specific LiDAR
 154 scanners are determined by the manufacturer. They performed 15 flight lines for YSM+ and 13 for YSM at
 155 velocities between 5 and 10 m/s and between heights between 50 and 120 m.a.g.l. over a series of
 156 surfaces. The assessment with 18 ground truth points resulted in the values given in Table 1. All surveys
 157 in this study were performed within one year of the calibration. For both palsas, a flight with high overlap
 158 was done and supported by a second flight with additional orthogonal trajectories. The same flight plans
 159 were executed for all five scanings to ensure equal spatial coverage and resolution.



160
 161 **Figure 3. DJI Matrice 300 RTK equipped with the YellowScan Mapper + in front of the Ridge palsa.**

162 The April 2023 flights were performed during a period of snowmelt, so that parts of both palsas were snow-
 163 free, while other parts remained snow-covered. Consequently, in order to investigate changes in terrain
 164 elevation, the snow-free parts needed to be isolated for analysis. For that reason, flights with a second UAV
 165 (DJI Phantom 4 Pro v2.0) with an RGB camera to create orthomosaics were performed on the same day
 166 as the LiDAR scanning.

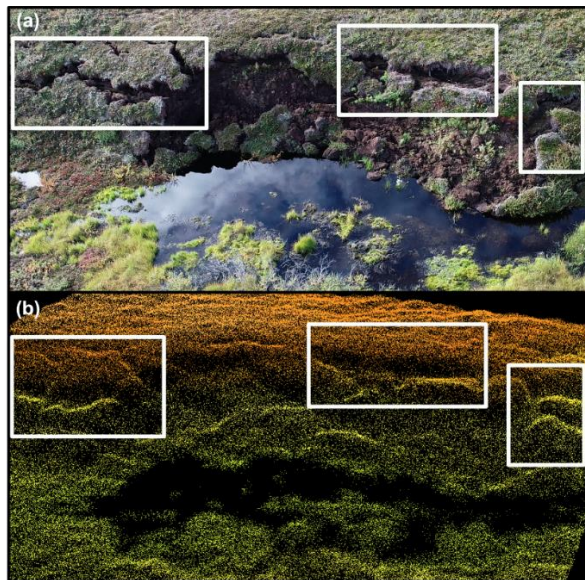
167 **Table 1. LiDAR scanner and flight parameters of the flight missions. Where values for YellowScan Mapper**
 168 **differ from YellowScan Mapper +, they are shown within parentheses.**

Parameter	Value, YellowScan Mapper + (Mapper)
Vertical Accuracy (RMSE, m)	0.021 (0.028)
Precision (m)	0.024 (0.032)
Number of returns	3 (2)

Altitude (m.a.g.l.)	60
Velocity (m/s)	8
Overlap (%)	60

169

170 Regarding the UAV LiDAR flights, the average flight time was 6 minutes and 49 seconds over the Dome
 171 palsa, and slightly shorter over the Ridge palsa at 5 minutes and 13 seconds. Similarly, flights over the
 172 Dome palsa yielded a slightly larger coverage area of 53993 m² compared to the Ridge palsa, which
 173 covered an area of 42072 m², including part of the surrounding mire and forested mountain. The mean
 174 point densities over the Dome palsas were 1327 (YSM) and 1462 (YSM+) points/m², and 1201 (YSM) and
 175 1519 (YSM+) points/m² at the Ridge palsa. These pulse densities can be regarded as very high, easily
 176 allowing the creation of DTMs with high spatial resolution. Terrain features such as surface cracks and
 177 blocks of peat are well-identifiable in the LiDAR point cloud data, which emphasizes the high quality of the
 178 collected data (Fig. 4).



179

180 **Figure 4. (a) RGB photo of a degrading edge and formation of a thermokarst lake at the Dome palsa, taken with**
 181 **a DJI Phantom 4 UAV in September 2022. (b) Dense UAV LiDAR point cloud taken on the same day with the**
 182 **DJI Matrice 300 RTK equipped with the YellowScan Mapper. Morphological features such as cracks in the**
 183 **surface and individual blocks of peat can clearly be recognized in the point cloud. This section of the palsa**
 184 **reaches a height of ca. 4 meters.**

185 3.2 Point cloud processing and DTM creation

186 The processing of a LiDAR point cloud requires several steps, including GPS correction, strip adjustment,
187 classification of ground points, and the creation of a DTM raster. The position data captured by the LiDAR
188 system during the flights were postprocessed in PosPac UAV v. 8.2 (*PosPac UAV*, 2023) using PP-RTX
189 for trajectory correction. PP-RTX for UAV uses the Trimble CenterPoint® RTX™ correction service, which
190 computes corrections to satellite orbit and clock data for trajectory correction and positioning, based on a
191 global network of tracking stations. This cloud-based solution gives centimeter-level positioning accuracy
192 without the requirement to set up a local base, which makes PP-RTX particularly advantageous for UAV
193 surveys in remote regions. YellowScan's processing software, CloudStation (*CloudStation*, 2023), was then
194 used for strip adjustment to reduce the relative adjustment error. The point clouds were compared visually
195 for alignment in areas where changes were least likely. Following this, CloudCompare v. 2.12.4
196 (*CloudCompare*, 2023) was used to perform the classification of points into ground and non-ground points
197 using the Cloth Simulation Filter (CSF) (Zhang et al., 2016). The CSF method simulates a virtual cloth
198 dropping onto the inverted point cloud. Points that are close to where the cloth settles are classified as
199 ground, while those that are farther away are considered non-ground. The software allows three adjustable
200 parameters for the CSF classification. Several parameter combinations were tested and the best result,
201 based on visual inspection of the resulting point cloud, was achieved with the following parameters: 'Cloth
202 resolution' = 0.10 m (matching the resolution of the created DTMs), 'Max iterations' = 500 and 'Classification
203 threshold' = 0.10 m (controlling the distance of points to be classified as ground), resulting in a detailed
204 ground surface. Only ground points were then used to create the DTM, and in this project a grid cell
205 resolution of 0.10 m was chosen. Since the total thickness of the point cloud along the ground was between
206 ca. 0.10 and 0.30 m, the minimum elevation per grid cell was used during the rasterization in order to ensure
207 that the raster represents the ground elevation. A comparison of the lowest point and the 25th percentile
208 elevation in 100 random 0.10 m by 0.10 m areas on each palsa was carried out, which showed no outliers
209 at the ground level. This process was carried out for all five time points, creating a DTM for each scanning
210 and palsa. Finally, the resulting DTMs were used for change detection by subtracting values of one raster
211 from another. For the change detection, the error range was calculated following the topographic error

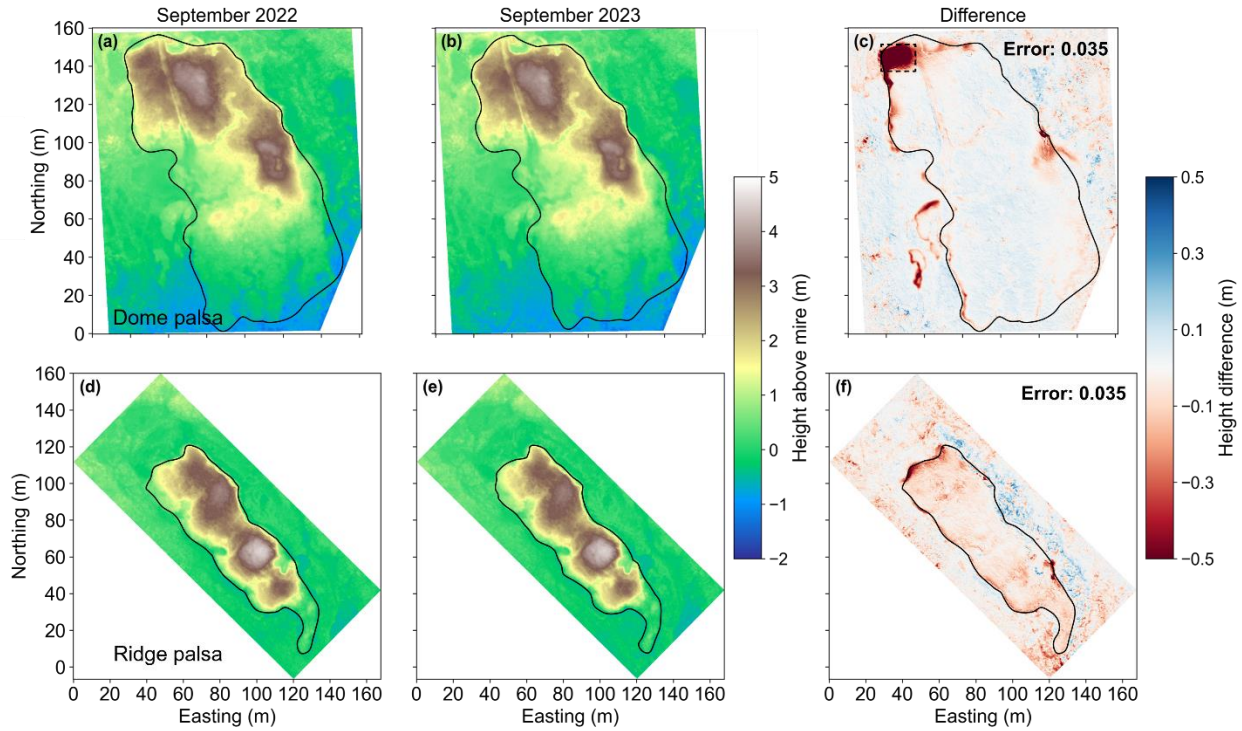
212 propagation law (Taylor, 1997), where the propagated error was described as the root sum of squares
213 (RSS) of individual errors. For the individual errors, those described in Table 1 were used.

214 The snow free parts of the palsas from the April 2023 data were singled out for the computation of heave
215 and subsidence. These areas were identified using georeferenced orthophotos taken on the same day in
216 April as the LiDAR data, in combination with a hillshade image from the DTM (since the hillshade is smooth
217 where there is snow). Orthophotos that were taken on the same day as the LiDAR surveys in September
218 2022 and September 2023 were used to determine the extent of the palsas. For each DTM, the mean
219 elevation of the palsa's surrounding was computed and subtracted from the DTM, which normalizes the
220 elevation of the palsa into the height above the surroundings. Since the definition of palsas is morphological
221 (Harris et al., 1988), the height above its surroundings is per definition the height of the palsa. For the
222 normalization, we used the previously mentioned orthophotos to create a polygon around each palsa, for
223 which the mean elevation was taken per LiDAR flight. Areas containing open water at any of the time steps,
224 either thermokarst lakes directly around the palsas or other ponds, were not included in these polygons.
225 The transformation from elevation to height, simplifies the comparison between the data from the different
226 flights. Since the mire in April was snow-covered, the mire elevation from the closest date (June) was taken
227 for normalizing the April DTM.

228 **4 Results**

229 **4.1 Annual terrain changes from UAV LiDAR**

230 Between September 2022 and September 2023, both palsas underwent degradation along their margins
231 (Fig. 5). The largest height change was observed along the northwest edge of the Dome palsa, where an
232 area of 225 m² (2.6% of the total palsa area) subsided up to 1.9 m and on average 0.85 m. This corresponds
233 to a 34% height loss on this part of the palsa. From hereon we name this 225 m² area the 'degradation
234 hotspot'. Degradation also occurred within the ATV track that borders the eastern side of this degradation
235 hotspot. The height of the Ridge palsa decreased slightly over the entire landform, with most loss along the
236 margins in the form of lateral degradation.



237

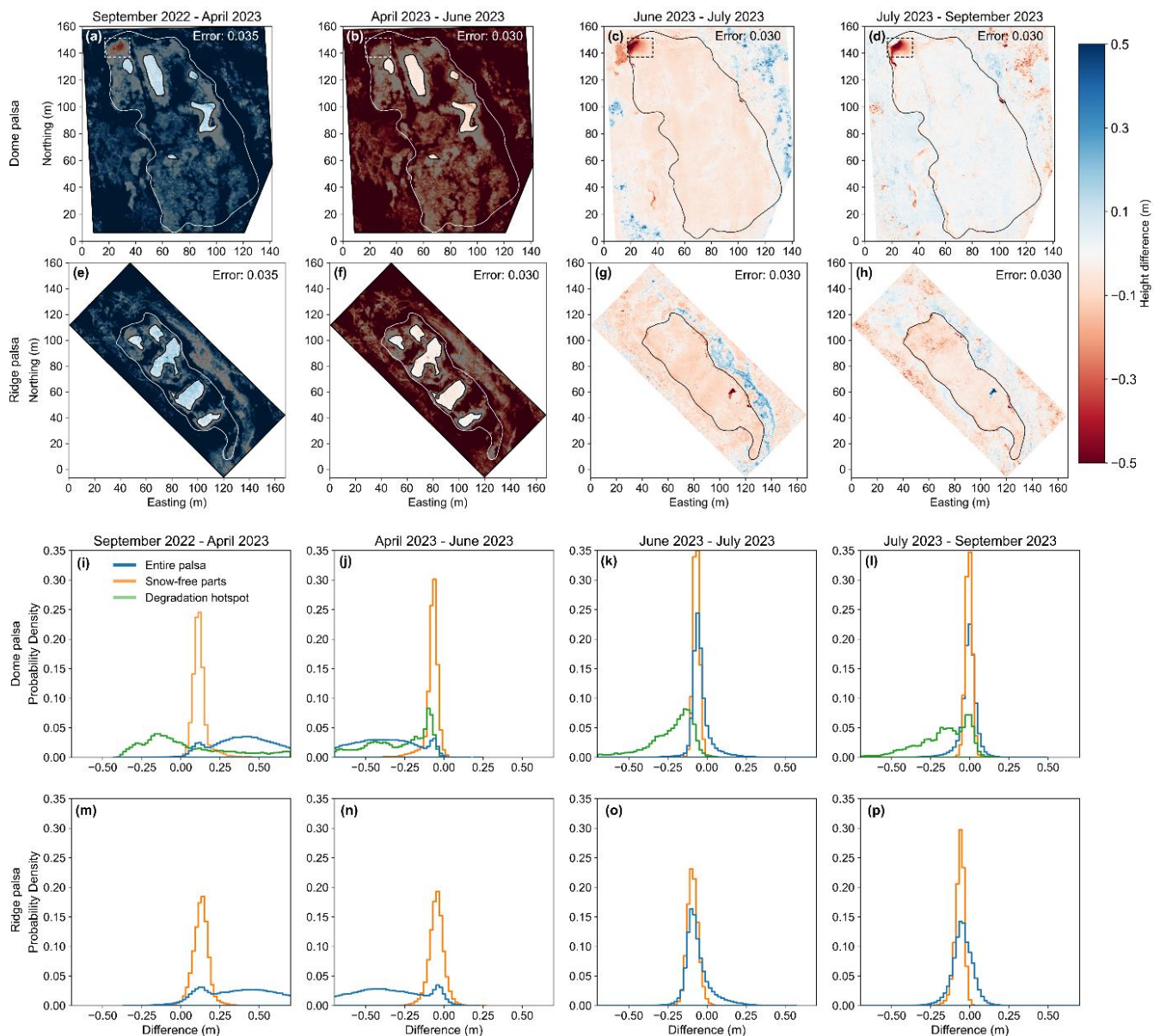
238 **Figure 5. DTMs of the Dome (a,b) and Ridge (d,e) palsas on UAV LiDAR scans in September 2022 and**
 239 **September 2023. The black lines represent the extent of the palsas, based on orthomosaics from the same day**
 240 **as the UAV LiDAR surveys. The difference maps (c,f) show the topographical changes over one year, with the**
 241 **palsa extent from the September 2022 orthomosaics in black. The dashed box in (c) shows the ‘degradation**
 242 **hotspot’ on the Dome palsa.**

243 **4.2 Seasonal terrain changes from UAV LiDAR**

244 By comparing DTMs from consecutive periods, we observed intra-annual terrain variations, i.e. frost heave
 245 and thaw subsidence on the two studied palsas. Change maps for the different time steps are shown in
 246 Figs. 6a–h, while Figs. 6i–p are corresponding histograms of change. The first two time steps are largely
 247 affected by snow cover in April, hence the histograms of change show both the entire palsa as well as only
 248 the snow-free parts (Figs. 6i–p).

249 On the snow-free crests there was an elevation increase (heave) of up to 0.30 m and on average of 0.15
 250 m from September 2022 to April 2023 for both palsas (Figs. 6a and 6e). Between June and July, both
 251 palsas clearly subside over the whole area (Figs. 6c and 6g), on average 0.05 m on the Dome palsa and

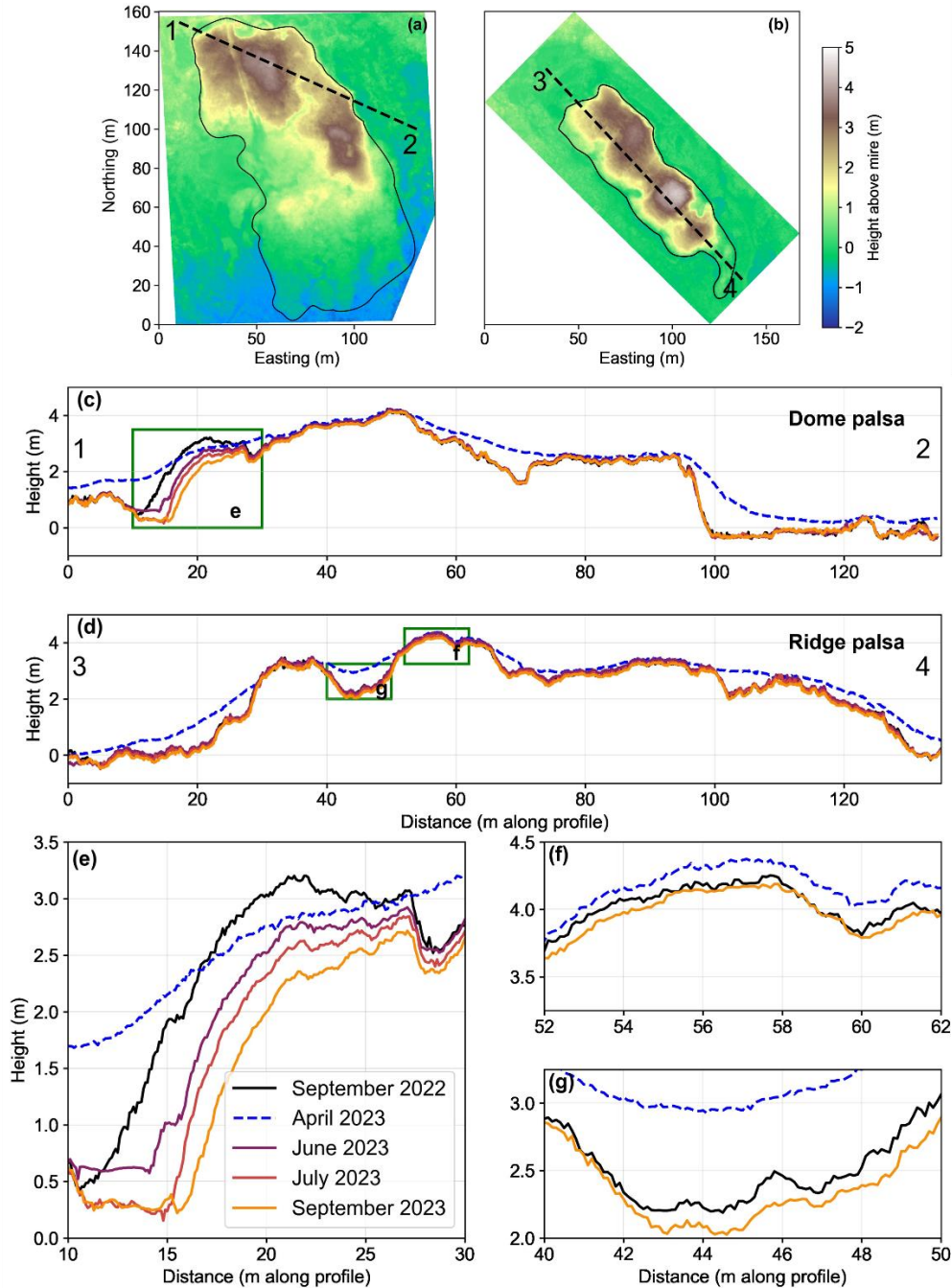
252 0.08 m on the Ridge palsa. Subsidence from July to September is only clear on the Ridge palsa, with 0.05
 253 m on average over the entire palsa (Fig. 6h). Despite being snow-covered in April, the degradation hotspot
 254 in the northwestern part of the Dome Palsa displayed a height decrease of up to 0.4 m between September
 255 2022 and April 2023 (Fig. 6a and 6i), indicating that subsidence in this area occurred between these months.
 256



257
 258 **Figure 6. Sequential height difference maps of the Dome (a,b,c,d, with the ‘degradation hotspot’ in the dashed**
 259 **rectangles) and Ridge (e,f,g,h) palsas between the five UAV LiDAR DTMs from September 2022 to September**

260 **2023. Each panel showcases the topographical changes over successive intervals. Blue colors indicate**
261 **elevation gains and red colors indicate elevation losses. The snow-covered areas (a, b, e, f) are greyed out,**
262 **leaving the snow-free parts highlighted. Panels i–p display histograms with the distribution of height changes,**
263 **separated into the entire palsa area (including snow-free parts), snow-free parts only, and the 'degradation**
264 **hotspot' on the Dome palsa.**

265 Figure 7 shows a time series of elevation changes along profiles, providing another way to look at the heave
266 and subsidence. The degradation hotspot is seen in Figs. 7c and 7e, where this area progressively
267 degraded vertically up to 1.9 m between September 2022 and September 2023. The ATV track that crosses
268 the Dome palsa shows a subsidence of 0.2–0.3 m just over the time period in this study (at ca. 27–29 m in
269 Fig. 7e). On the Ridge palsa it can be seen in Figs. 7f and g that the subsidence was greater in the
270 depressions than on the crests. The heterogeneous snow cover is visible in Figs. 7c and d. The snow
271 thickness is up to ca. 2.0 m at the eastern margin of both palsas and 1.0 to 1.5 m in the depressions, while
272 the crests remain snow-free (also see Fig. 1d).



273

274

275

276

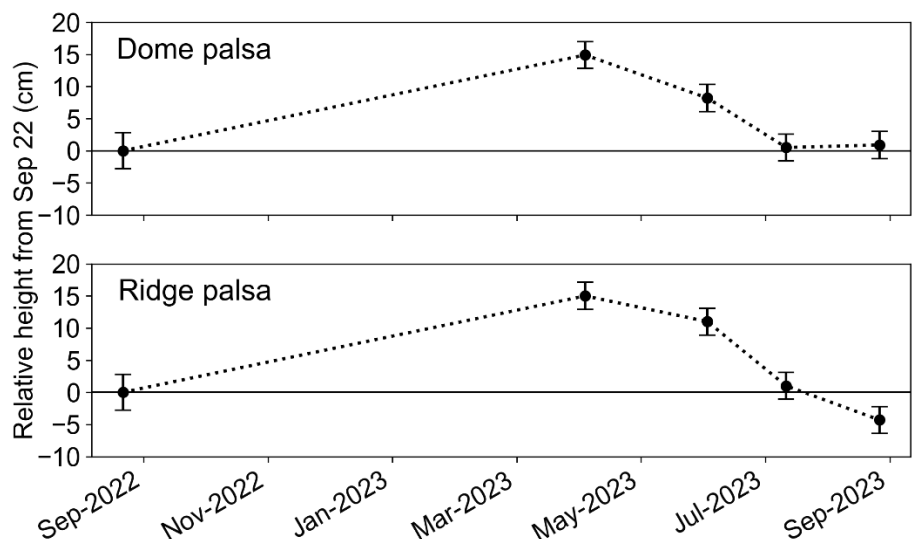
277

278

279

Figure 7. Elevation profiles of the Dome and Ridge palsa based on UAV LiDAR DTMs from September 2022 to September 2023. (a,b) September 2022 DTMs with the corresponding palsa outline. The dashed lines denote the location of the elevation profiles 1–2 and 3–4. (c) and (d) provide a general elevation overview of the transect, while (e), (f), and (g) offer zoomed-in views of specific areas of interest, indicated by the green boxes. The profile from April 2023 is mostly showing the snowpack, although some peaks are snow-free (see also Fig. 1d).

280 The mean height of both palsas, calculated by taking all pixels within the snow-free areas, increased 0.15
 281 m between September 2022 and April 2023 (Fig. 8). The subsequent flights throughout the summer season
 282 show a successive lowering of the palsa height, i.e. subsidence. As shown in Fig. 6, the rate of subsidence
 283 is highest between the June and July flights. The Dome palsa returned to a similar mean height in
 284 September 2023 as compared to September 2022, while the snow-free parts on the Ridge palsa subsided
 285 to a 0.04 m lower mean height in September 2023 than in September 2022, which is also shown in Fig. 5.
 286 Overall, the heave and subsidence pattern is very similar across the two studied palsas.



287
 288 **Figure 8. Heave and subsidence on the two studied palsas during the 2022-2023 year. Mean height changes**
 289 **relative to September 2022 are plotted (only for the areas that were completely snow-free in April 2023). The**
 290 **cumulative changes of the intermediate steps add up to the total change from September 2022 to September**
 291 **2023. The error bars represent the scanner specific RMSE for the respective LiDAR scanners used.**

292

293 **5 Discussion**

294 **5.1 Intra-annual heave and subsidence on palsas**

295 The objective of this study was to elucidate and quantify the intra-annual dynamics of two large palsas in
296 the Vissátvuopmi palsa mire, and to achieve this, the use of UAV LiDAR proved to be an extremely suitable
297 tool. Analysis of the DTMs indicated that both palsas had frost heave of ca. 0.15 m on average between
298 September and April, and subsequent thaw subsidence from April to September. This is the first study that
299 covers these dynamics on palsas in such high spatial resolution, although seasonal terrain variability has
300 been investigated in other permafrost environments (Gruber, 2020; Hu et al., 2022; Iwahana et al., 2021;
301 Lin et al., 2019). For example, the heave and subsidence detected in this study are similar to values (0.10
302 – 0.14 m) observed in the GNSS positioning survey by Iwahana et al. (2021) on an intact tundra site in
303 Alaska after the warm summer of 2019.

304 The largest rate of subsidence in our study occurred between June and July 2023, which was 0.05 m on
305 the Dome palsa and 0.08 m on the Ridge palsa. Freeze-thaw cycles within the active layer cause frost
306 heave and thaw subsidence, partially due to the density difference between water and ice. However, the
307 average observed heave of 0.15 m cannot be explained alone by this process and requires the formation
308 of seasonal segregation ice (i.e. ice lenses) within the active layer (Fu et al., 2022; Iwahana et al., 2021).
309 Alternatively, processes within the core of the palsa, for example, the infiltration and refreezing along
310 meltwater pathways, might result in seasonal heave and subsidence. To make more conclusive statements
311 about the exact mechanisms, it would be necessary to obtain complementary observations from the interior
312 of these palsas, in the form of soil and ice cores. Taking this step in the future would allow the observed
313 changes in the terrain morphology such as those done here to be better understood in relation to internal
314 palsa dynamics.

315 The 0.15 m heave is computed on the areas that were snow-free in April and are thus biased towards the
316 crests of the palsas that have a thinner active layer (see Appendix A) as they have a thinner winter snow
317 cover, which limits the insulation of the ground below. Since the magnitude of the heave and subsidence
318 depends on the thickness of the active layer (Iwahana et al., 2021), the areas with a deeper active layer

319 (i.e. those not included in the computation due to remaining snow in April) are therefore expected to have
320 undergone an even larger increase in height between September 2022 and April 2023. A process other
321 than freeze-thaw dynamics that could have affected the LiDAR measurements is the seasonal oscillation
322 of the peatland surface height due to water table fluctuations, called 'mire breathing' (Kellner & Halldin,
323 2002; Roulet, 1991). By accounting for the elevational changes in the ground surface of the surrounding
324 mire (and thus not open water), we ensure that the presented height values reflect height of the palsa
325 mounds and thus hold true to the morphological definition of palsas. Since palsa mires are very dynamic
326 landscapes, each correction brings uncertainties. The closely aligned elevation profiles (Fig. 7) give us
327 confidence that the presented height changes are primarily a result of freeze-thaw dynamics of the palsas.

328 While other studies have applied multitemporal LiDAR for detecting permafrost dynamics, they have used
329 terrestrial LiDAR scanning (Anders et al., 2020) rather than UAV-borne LiDAR, or else inter-annual airborne
330 LiDAR (e.g. Douglas et al., 2021; Jones et al., 2015), which generally has meter-scale spatial resolutions
331 and infrequent revisit periods. Anders et al. (2020) performed three TLS measurements over 14 months
332 (June 2015, Aug 2015, and Aug 2016) to observe thaw subsidence of a permafrost area in Northwest
333 Territories, Canada, finding a total change of 1.4 cm; they determined that the TLS measurements were
334 more accurate than those from field-based surveying. While promising, the mobility and range of UAV
335 LiDAR is particularly advantageous when surveying permafrost features in peat- or wetland landscapes.

336 Another approach to quantify longer-term subsidence and the effect of seasonal freeze/thaw dynamics on
337 topography is through the use of InSAR remote sensing (de la Barreda-Bautista et al., 2022; Kou et al.,
338 2021; Valman et al., 2024; Yanagiya et al., 2023), which can be an effective method to detect the signal of
339 subsidence. de la Barreda-Bautista et al. (2022) reported a maximum subsidence rate of 1.5 cm, from
340 InSAR data between 2017 and 2020 on a palsa plateau ca. 100 km from the Vissátvuopmi palsa complex.
341 Due to the coarser grid cell size (20 m) of the resulting data, it is likely to underestimate actual heave and
342 subsidence values of smaller isolated features such as palsas. Over the same period and location, they
343 observed 25 cm subsidence from DEMs created with UAV photogrammetry. InSAR subsidence has also
344 been analyzed at the Vissátvuopmi palsa complex (Valman et al., 2024). They found that Vissátvuopmi and
345 the adjacent Árbuvuopmi are the fastest subsiding complexes of the eight studied in northern Sweden, with

346 maximum subsidence rates of -8.9 and -9.9 mm yr⁻¹ between 2017 and 2021. While the absolute values
347 are not comparable with subsidence rates from our UAV LiDAR data, possibly due to the larger grid cell
348 size from InSAR analysis, they give an important context of the subsidence trend across the entire palsa
349 complex in the years right before our study period. The fact that Vissátvuopmi is among the most quickly
350 deforming complexes and at the same time does not hold a protected status, emphasizes the importance
351 of studies conducted here.

352 In our study, we show that the elevation change of the Dome palsa as a whole from September 2022 to
353 September 2023 was minor and mostly within the 0.030 m error range, while the Ridge palsa did subside
354 on average 0.07 m within one year. A hypothesis for this is related to the surrounding thermokarst ponds.
355 The Ridge palsa is surrounded by relatively larger and deeper thermokarst ponds, which could enhance
356 vertical subsidence more centrally in the palsas as a result of increased heat transfer to the palsa core. To
357 find out if the higher subsidence on this palsa is a robust signal and what processes are responsible for
358 this, continued annual LiDAR surveys and observations of the palsa's interior via geophysical imaging are
359 needed.

360 **5.2 Lateral palsa degradation**

361 The time series from this study showed not only the seasonal heave and subsidence patterns, but also
362 revealed a degradation hotspot on the Dome palsa that happened between September 2022 and April
363 2023. By comparing the elevation profiles and histograms of change for these two timestamps at the
364 degradation hotspot (Fig. 7e and Fig. 6i), we can see that a drop of up to 0.4 m happened within the autumn
365 and/or winter season, despite the presence of a snow cover in April. It is important to consider that positive
366 air temperatures persisted until the end of October 2022 (Fig. 2), which suggests that the subsidence likely
367 continued into the late autumn 2022 period, influenced by prolonged thawing conditions. Whether this entire
368 drop in palsa height occurred solely between the September 2022 campaign and the freeze-up of the entire
369 active layer, or if gravitational processes also contributed after the complete freeze-up, remains uncertain.
370 Regarding the initiation of the degradation at this location, it is likely that it was ongoing earlier in the summer
371 of 2022. Both the air temperatures (>20 °C) and precipitation (158 mm) (both measured at Saarikoski

372 weather station) peaked in July of that year, which could have resulted in a deeply thawed, saturated upper
373 layer of the palsa and initiated a progressive lateral degradation event. Additionally, the precipitation in this
374 winter was greater than the previous winter, which may have caused additional warming of the ground,
375 either via a thicker snowpack (Zhang, 2005) or latent heat brought by rainfall (Putkonen & Roe, 2003). This
376 falls in line with Olvmo et al. (2020), who conclude that increased winter precipitation is one of the main
377 causes of rapid palsa degradation in the study region.

378 The characteristic of this degradation hotspot is similar to that described in Martin et al. (2021) as “constant
379 edge degradation”, which they found as the second phase of lateral degradation on peat plateaus following
380 “initial slope adjustment” and preceding “plateau collapse” phases. While both the spatial and temporal
381 scale differ between their and our study, this could indicate that a more widespread collapse or subsidence
382 can follow on the Dome palsa. As described in Valman et al. (2024), approaches that identify initial signs
383 of permafrost degradation with the use of repeated measurements are needed, to which our study adds. In
384 order to make more conclusive statements about the reason for this rapid degradation, the monitoring of
385 ground temperatures and knowledge of the internal structure of this palsa is required. The degradation
386 hotspot could be just an isolated event, or a precursor to rapid degradation in the following years.

387 Olvmo et al. (2020) found an average annual decay rate (loss of palsa area) of $-0.74\%a^{-1}$ and $-2.45\%a^{-1}$
388 for the Dome and Ridge palsas respectively, for the period 2010–2016. Using the palsa area from Olvmo
389 et al. (2020) in 2016 and the extent in 2023 from our study, we can calculate a new annual decay rate. For
390 the period 2016–2023, we found respective rates of $-3.27\%a^{-1}$ and $-1.55\%a^{-1}$. The $-2.53\%a^{-1}$ change in
391 decay rate on the Dome palsa can be largely explained by the degradation hotspot, which covered ca. 2.6%
392 of the total palsa area. The slight decrease in annual decay rate on the Ridge palsa could be explained by
393 a stabilization of degraded areas. When excluding the degradation hotspot on the Dome palsa, the Ridge
394 palsa lost a larger percentage of its extent, similar to Olvmo et al. (2020). Again, lateral water fluxes greatly
395 affect ground temperatures and permafrost degradation (Martin et al., 2021; Sjöberg et al., 2016; Walvoord
396 & Kurylyk, 2016). Therefore, smaller palsas are relatively more susceptible to lateral erosion through heat
397 and water fluxes, provided by surrounding thermokarst ponds, compared to larger palsas (e.g. Borge et al.,
398 2017).

399 **5.3 Using UAV LiDAR to monitor permafrost landscapes**

400 The use of UAVs in assessing permafrost landscapes has increased in recent years (e.g. de la Barreda-
401 Bautista et al., 2022; Krutskikh et al., 2023; Martin et al., 2021; Siewert & Olofsson, 2020; Sjögersten et al.,
402 2023; Verdonen et al., 2023), although primarily with the use of photogrammetry. Changes in the exterior
403 of permafrost peatlands can be subtle and therefore require the use of highly accurate methods of
404 measuring ground elevation, particularly for vertical subsidence, and when studied over relatively short
405 timescales.

406 A challenge in permafrost environments, especially palsa mires, is the lack of stable elevation points to be
407 used for ground control points (GCPs). In this study, GCPs were not used, however, all point clouds were
408 obtained using GNSS, post-processed as described in 3.2, and visually checked over the whole scanned
409 area for consistency. The elevation profiles (Fig. 7) from the five campaigns are well-aligned and thereby
410 confirm that the positional data are highly accurate. As mentioned by Harder (2020), the use of GCPs is
411 not strictly necessary for UAV LiDAR applications, which significantly contributes to the efficient field visits
412 in harsh Arctic conditions.

413 In this study, we employed the YellowScan Mapper (YSM) system in September 2022 and the YellowScan
414 Mapper + (YSM+) in the four campaigns in 2023. The use of an upgraded LiDAR system after the first
415 scanning introduces a potential source of uncertainty in our measurements. However, both systems
416 achieved high point densities ($>1,000$ points/m²), ensuring detailed surface representation in both datasets
417 despite the difference in the number of recorded returns per pulse. Furthermore, the alignment and
418 positioning of the data were visually verified, showing that the impact of using different systems on our
419 results is minimal. The vertical accuracy of the YSM and YSM+ systems used here have an RMSE of 2.8
420 and 2.1 cm, respectively. This is a potential error source in the data and changes less than the propagated
421 error (See Fig. 6a–h) are within the margin of error. The main findings of the study, which include the
422 observed 0.15 m mean heave in winter and associated subsidence over summer and the identification of a
423 degradation hotspot, are larger than the described error. Both YellowScan LiDAR systems have a minimum
424 distance of 1 m between registered returns at a flying height of 60 m. This means that all objects on the
425 surface shorter than 1 m in height will be measured by a single return. In this case, to measure the ground

426 elevation underneath vegetation cover requires high point density, which was acquired in this study. By
427 using the minimum elevation per grid cell, the resulting DTM should exclude vegetation heights. In our
428 study, the diffuse cover of *Betula nana* ranged from 0-100% per m² over both palsas, yet the ground could
429 almost always be seen between the sparse branches. Careful consideration of acquisition parameters and
430 algorithms is needed when UAV LiDAR is to be used to create DTMs in areas of extremely dense vegetation
431 cover, or when small grid cell sizes are needed to allow determination of the ground elevation (Kucharczyk
432 et al., 2018).

433 The ability of LiDAR instruments to measure ground elevation below the vegetation canopy is one of the
434 major advantages that LiDAR has over photogrammetry. Fig. 3 shows, for example, the Ridge palsa with
435 several large birch trees, where terrain analysis can still be done below the canopy. Photogrammetry
436 creates surface models that consist of vegetation height, which is likely to increase over the vegetation
437 season, adding bias to the models. The observed frost heave and subsidence in our study would not have
438 been soundly established with just the use of photogrammetrically-derived surface models, due to the
439 potential confusion between vegetation and ground height. A disadvantage when comparing LiDAR and
440 photogrammetric methods is the higher costs of UAV LiDAR scanners at the present time. For that reason
441 alone, when one's objective is to merely compare the perimeter of palsas (e.g, lateral degradation) or other
442 landforms with low-growing vegetation, photogrammetry might still be preferred. While some UAV LiDAR
443 systems can also be integrated with an RGB camera, due to the additional costs, this was not done in this
444 study. The main advantage that this would give is an improved visualization through use of colorized point
445 clouds and could thereby improve the delineation of, for example, snow-covered (or -free) areas. UAVs
446 present several advantages over 'classic' airborne LiDAR surveys, including higher spatial resolution DTMs,
447 simpler planning, and reduced costs, particularly for smaller spatial extents. Additionally, the increased
448 temporal frequency achievable with UAVs enables more frequent data acquisition, which is essential for
449 monitoring intra-annual dynamics in permafrost landscapes.

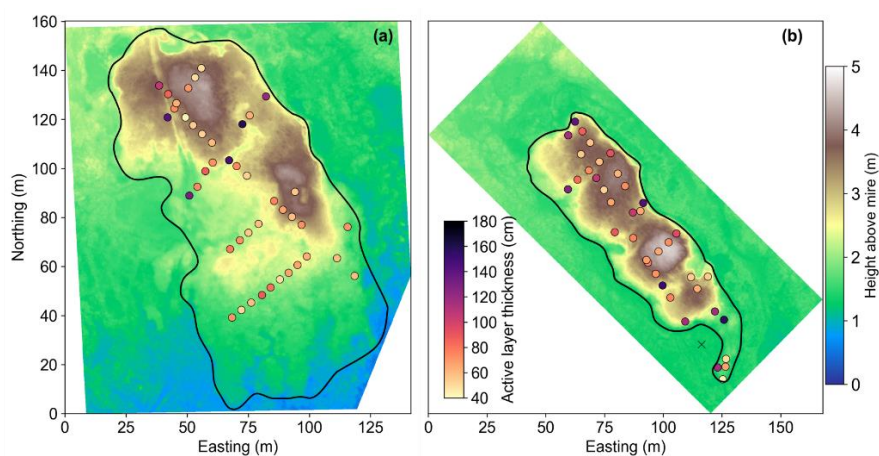
450 **6 Conclusions**

451 This study has provided insights into the intra-annual dynamics of palsas through the use of repeat UAV
452 LiDAR measurements, which we highlight as an effective tool for detailed change detection in permafrost
453 landscapes. We present a unique time series of five UAV LiDAR campaigns during a one-year time span
454 on two large palsas in Sweden's largest coherent palsa mire complex. The study revealed seasonal
455 variations in the palsas' topography, with an average frost heave and thaw subsidence of 0.15 m (and up
456 to 0.30 m), with the highest rate of subsidence on the palsas between June and July. The time series also
457 shows a considerable lateral degradation hotspot in a 225 m² section of one of the palsas, with a subsidence
458 of up to 1.9 m over the one-year study period. This substantial permafrost degradation occurred between
459 September 2022 and April 2023 which suggests that the degradation of palsas is not limited to the summer
460 months. To conclude, the use of repeat UAV LiDAR scanning has proven to be a highly effective tool for
461 capturing detailed seasonal measurements of permafrost dynamics, which would not have been observed
462 if only annual measurements had been taken.

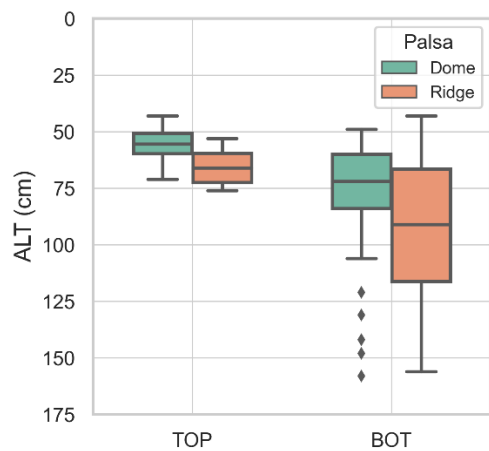
463

464 **Appendix A: Active layer thickness**

465 The thickness of the active layer (ALT) is measured in September 2023 at both the Dome and the Ridge
466 palsas by inserting a 1.80 m steel rod until the top of the frozen ground was met. The points (Fig. A1) are
467 either within the polygons of the parts that were snow-free in April 2023 (see Figs. 6a, b, d and e) or in a
468 lower part of the palsa. The former points are assigned 'TOP', while the latter are assigned 'BOT'. The
469 points in the 'TOP' class have a thinner and more narrowly spread ALT compared to the points in the 'BOT'
470 class (Fig. A2).



471
472 **Figure A1. Active layer thickness (ALT) on the Dome palsa (a) and Ridge palsa (b) in September 2023 with their**
473 **corresponding DTMs.**



474
475 **Figure A2. Distribution of the ALT at both palsas, showing that ALT in the top-positions is generally lower and**
476 **more narrowly spread compared to the points in the lower parts or depressions.**

478 **Data availability**

479 The data presented in this article are stored at <https://zenodo.org/records/10497094> (Renette., 2024).

480 **Author contribution**

481 CR and HR designed the study and performed the UAV surveys. HR acquired funding. CR handled data
482 processing, analysis, and figure creation. ST and BH assisted in the setup of the weather station. MO and
483 BH contributed expertise and advice. The manuscript was initially prepared by CR, assisted by HR. All
484 authors reviewed and edited the manuscript draft. All authors approved the final version for submission.

485 **Competing interests**

486 The authors declare that they have no conflict of interest.

487 **Acknowledgements**

488 This work was supported by the Swedish Research Council Formas (grant number 2022-00959),
489 “Threatened subarctic palsa mires: a new integrated approach to map and understand permafrost
490 degradation”. Also, we thank all those that helped with fieldwork and logistics. Finally, we would like to
491 thank reviewers Jan Henrik Blöthe and Martha Ledger for their valuable comments and suggestions, which
492 significantly improved the quality of the manuscript.

493

494

495 **References**

- 496 Anders, K., Marx, S., Boike, J., Herfort, B., Wilcox, E. J., Langer, M., Marsh, P., & Höfle, B. (2020).
497 Multitemporal terrestrial laser scanning point clouds for thaw subsidence observation at Arctic
498 permafrost monitoring sites. *Earth Surface Processes and Landforms*, *45*(7), 1589–1600.
499 <https://doi.org/10.1002/esp.4833>
- 500 Andersson, L., Rafstedt, T., & von Sydow, U. (1985). *FJALLENS VEGETATION Norrbottens län: En*
501 *översikt av Norrbottenfjällens vegetation baserad på vegetationskartering och naturvärdering*.
502 Naturvårdsverket. <https://urn.kb.se/resolve?urn=urn:nbn:se:naturvardsverket:diva-7479>
- 503 Backe, S. (2014). *Kartering av Sveriges palsmyrar* (pp. 1–54) [Text].
504 [https://www.lansstyrelsen.se/norrboten/om-oss/vara-tjanster/publikationer/2014/kartering-av-](https://www.lansstyrelsen.se/norrboten/om-oss/vara-tjanster/publikationer/2014/kartering-av-sveriges-palsmyrar.html)
505 [sveriges-palsmyrar.html](https://www.lansstyrelsen.se/norrboten/om-oss/vara-tjanster/publikationer/2014/kartering-av-sveriges-palsmyrar.html)
- 506 Biskaborn, B. K., Smith, S. L., Noetzli, J., Matthes, H., Vieira, G., Streletskiy, D. A., Schoeneich, P.,
507 Romanovsky, V. E., Lewkowitz, A. G., Abramov, A., Allard, M., Boike, J., Cable, W. L.,
508 Christiansen, H. H., Delaloye, R., Diekmann, B., Drozdov, D., Etzelmüller, B., Grosse, G., ...
509 Lantuit, H. (2019). Permafrost is warming at a global scale. *Nature Communications*, *10*(1),
510 Article 1. <https://doi.org/10.1038/s41467-018-08240-4>
- 511 Borge, A. F., Westermann, S., Solheim, I., & Etzelmüller, B. (2017). Strong degradation of palsas and
512 peat plateaus in northern Norway during the last 60 years. *The Cryosphere*, *11*(1), 1–16.
513 <https://doi.org/10.5194/tc-11-1-2017>
- 514 *CloudCompare* (2.12.4). (2023). [Computer software]. GPL software.
515 <https://www.danielgm.net/cc/release/>
- 516 *CloudStation* (2309.0.0). (2023). [Computer software]. YellowScan.
517 <https://www.yellowscan.com/products/cloudstation/>
- 518 Curcio, A. C., Peralta, G., Aranda, M., & Barbero, L. (2022). Evaluating the Performance of High Spatial
519 Resolution UAV-Photogrammetry and UAV-LiDAR for Salt Marshes: The Cádiz Bay Study Case.
520 *Remote Sensing*, *14*(15), Article 15. <https://doi.org/10.3390/rs14153582>
- 521 de la Barrera-Bautista, B., Boyd, D. S., Ledger, M., Siewert, M. B., Chandler, C., Bradley, A. V., Gee, D.,
522 Large, D. J., Olofsson, J., Sowter, A., & Sjögersten, S. (2022). Towards a Monitoring Approach

523 for Understanding Permafrost Degradation and Linked Subsidence in Arctic Peatlands. *Remote*
524 *Sensing*, 14(3), Article 3. <https://doi.org/10.3390/rs14030444>

525 Douglas, T. A., Hiemstra, C. A., Anderson, J. E., Barbato, R. A., Bjella, K. L., Deeb, E. J., Gelvin, A. B.,
526 Nelsen, P. E., Newman, S. D., Saari, S. P., & Wagner, A. M. (2021). Recent degradation of
527 interior Alaska permafrost mapped with ground surveys, geophysics, deep drilling, and repeat
528 airborne lidar. *The Cryosphere*, 15(8), 3555–3575. <https://doi.org/10.5194/tc-15-3555-2021>

529 *EUNIS - Factsheet for Palsa mires*. (2013). Retrieved November 10, 2023, from
530 <https://eunis.eea.europa.eu/habitats/10155>

531 Fewster, R. E., Morris, P. J., Ivanovic, R. F., Swindles, G. T., Peregon, A. M., & Smith, C. J. (2022).
532 Imminent loss of climate space for permafrost peatlands in Europe and Western Siberia. *Nature*
533 *Climate Change*, 12(4), 373–379. <https://doi.org/10.1038/s41558-022-01296-7>

534 Fu, Z., Wu, Q., Zhang, W., He, H., & Wang, L. (2022). Water Migration and Segregated Ice Formation in
535 Frozen Ground: Current Advances and Future Perspectives. *Frontiers in Earth Science*, 10.
536 <https://www.frontiersin.org/articles/10.3389/feart.2022.826961>

537 Gruber, S. (2020). Ground subsidence and heave over permafrost: Hourly time series reveal interannual,
538 seasonal and shorter-term movement caused by freezing, thawing and water movement. *The*
539 *Cryosphere*, 14(4), 1437–1447. <https://doi.org/10.5194/tc-14-1437-2020>

540 Harder, P., Pomeroy, J. W., & Helgason, W. D. (2020). Improving sub-canopy snow depth mapping with
541 unmanned aerial vehicles: Lidar versus structure-from-motion techniques. *The Cryosphere*, 14(6),
542 1919–1935. <https://doi.org/10.5194/tc-14-1919-2020>

543 Harris, S., French, H., Heginbottom, J., Johnston, G., Ladanyi, B., Sego, D., & Everdingen, R. (1988).
544 *Glossary of Permafrost and Related Ground-Ice Terms*. <https://doi.org/10.4224/20386561>

545 Hu, Y., Wang, J., Li, Z., & Peng, J. (2022). Ground surface elevation changes over permafrost areas
546 revealed by multiple GNSS interferometric reflectometry. *Journal of Geodesy*, 96(8), 56.
547 <https://doi.org/10.1007/s00190-022-01646-5>

548 Hugelius, G., Loisel, J., Chadburn, S., Jackson, R. B., Jones, M., MacDonald, G., Marushchak, M.,
549 Olefeldt, D., Packalen, M., Siewert, M. B., Treat, C., Turetsky, M., Voigt, C., & Yu, Z. (2020).
550 Large stocks of peatland carbon and nitrogen are vulnerable to permafrost thaw. *Proceedings of*

551 *the National Academy of Sciences*, 117(34), 20438–20446.
552 <https://doi.org/10.1073/pnas.1916387117>

553 Iwahana, G., Busey, R. C., & Saito, K. (2021). Seasonal and Interannual Ground-Surface Displacement in
554 Intact and Disturbed Tundra along the Dalton Highway on the North Slope, Alaska. *Land*, 10(1),
555 Article 1. <https://doi.org/10.3390/land10010022>

556 Jacobs, J. M., Hunsaker, A. G., Sullivan, F. B., Palace, M., Burakowski, E. A., Herrick, C., & Cho, E.
557 (2021). Snow depth mapping with unpiloted aerial system lidar observations: A case study in
558 Durham, New Hampshire, United States. *The Cryosphere*, 15(3), 1485–1500.
559 <https://doi.org/10.5194/tc-15-1485-2021>

560 Jones, B. M., Grosse, G., Arp, C. D., Miller, E., Liu, L., Hayes, D. J., & Larsen, C. F. (2015). Recent Arctic
561 tundra fire initiates widespread thermokarst development. *Scientific Reports*, 5(1), Article 1.
562 <https://doi.org/10.1038/srep15865>

563 Kellner, E., & Halldin, S. (2002). Water budget and surface-layer water storage in a Sphagnum bog in
564 central Sweden. *Hydrological Processes*, 16(1), 87–103. <https://doi.org/10.1002/hyp.286>

565 Kou, X., Liu, X., Zhang, Y., Zhang, Y., Wang, T., & Yan, S. (2021). A Study on the Detection of
566 Deformation of Tuotuohe Area on the Qinghai-Tibet Plateau. *2021 IEEE International Geoscience
567 and Remote Sensing Symposium IGARSS*, 5362–5365.
568 <https://doi.org/10.1109/IGARSS47720.2021.9555061>

569 Krutskikh, N., Ryazantsev, P., Ignashov, P., & Kabonen, A. (2023). The Spatial Analysis of Vegetation
570 Cover and Permafrost Degradation for a Subarctic Palsa Mire Based on UAS Photogrammetry
571 and GPR Data in the Kola Peninsula. *Remote Sensing*, 15, 1896.
572 <https://doi.org/10.3390/rs15071896>

573 Kucharczyk, M., Hugenholtz, C. H., & Zou, X. (2018). UAV–LiDAR accuracy in vegetated terrain. *Journal
574 of Unmanned Vehicle Systems*, 6(4), 212–234. <https://doi.org/10.1139/juvs-2017-0030>

575 Lantmäteriet. 2021. GSD-Orthophoto. Available from [https://www.lantmateriet.se/sv/Kartor-och-
576 geografisk-information/geodataprodukter/produktlista/ortofoto/](https://www.lantmateriet.se/sv/Kartor-och-geografisk-information/geodataprodukter/produktlista/ortofoto/) [accessed 1 Nov 2023].

577 Łakomiec, P., Holst, J., Friberg, T., Crill, P., Rakos, N., Kljun, N., Olsson, P.-O., Eklundh, L., Persson, A.,
578 & Rinne, J. (2021). Field-scale CH₄ emission at a subarctic mire with heterogeneous permafrost
579 thaw status. *Biogeosciences*, 18(20), 5811–5830. <https://doi.org/10.5194/bg-18-5811-2021>

580 Lin, Y.-C., Cheng, Y.-T., Zhou, T., Ravi, R., Hasheminasab, S. M., Flatt, J. E., Troy, C., & Habib, A.
581 (2019). Evaluation of UAV LiDAR for Mapping Coastal Environments. *Remote Sensing*, 11(24),
582 Article 24. <https://doi.org/10.3390/rs11242893>

583 Luoto, M., Fronzek, S., & Zuidhoff, F. S. (2004a). Spatial modelling of palsa mires in relation to climate in
584 northern Europe. *Earth Surface Processes and Landforms*, 29(11), 1373–1387.
585 <https://doi.org/10.1002/esp.1099>

586 Luoto, M., Heikkinen, R. K., & Carter, T. R. (2004b). Loss of palsa mires in Europe and biological
587 consequences. *Environmental Conservation*, 31(1), 30–37.
588 <https://doi.org/10.1017/S0376892904001018>

589 Mamet, S. D., Chun, K. P., Kershaw, G. G. L., Loranty, M. M., & Peter Kershaw, G. (2017). Recent
590 Increases in Permafrost Thaw Rates and Areal Loss of Palsas in the Western Northwest
591 Territories, Canada: Non-linear Palsa Degradation. *Permafrost and Periglacial Processes*, 28(4),
592 619–633. <https://doi.org/10.1002/ppp.1951>

593 Martin, L. C. P., Nitzbon, J., Scheer, J., Aas, K. S., Eiken, T., Langer, M., Filhol, S., Eitzelmüller, B., &
594 Westermann, S. (2021). Lateral thermokarst patterns in permafrost peat plateaus in northern
595 Norway. *The Cryosphere*, 15(7), 3423–3442. <https://doi.org/10.5194/tc-15-3423-2021>

596 Olvmo, M., Holmer, B., Thorsson, S., Reese, H., & Lindberg, F. (2020). Sub-arctic palsa degradation and
597 the role of climatic drivers in the largest coherent palsa mire complex in Sweden (Vissátvuopmi),
598 1955–2016. *Scientific Reports*, 10(1), Article 1. <https://doi.org/10.1038/s41598-020-65719-1>

599 Ostrowski, W., Górski, K., Pilarska, M., Salach, A., & Bakula, K. (2017). Comparison of the laser scanning
600 solutions for the unmanned aerial vehicles. *Archiwum Fotogrametrii, Kartografii i Teledetekcji*, 29,
601 101–123. <https://doi.org/10.14681/afkit.2017.008>

602 Pirk, N., Aalstad, K., Mannerfelt, E. S., Clayer, F., de Wit, H., Christiansen, C. T., Althuizen, I., Lee, H., &
603 Westermann, S. (2024). Disaggregating the Carbon Exchange of Degrading Permafrost

604 Peatlands Using Bayesian Deep Learning. *Geophysical Research Letters*, 51(10),
605 e2024GL109283. <https://doi.org/10.1029/2024GL109283>

606 POSPac UAV (8.2). (2023). [Computer software]. Applanix. [https://www.applanix.com/products/pospac-](https://www.applanix.com/products/pospac-uav.html)
607 [uav.html](https://www.applanix.com/products/pospac-uav.html)

608 Putkonen, J., & Roe, G. (2003). Rain-on-snow events impact soil temperatures and affect ungulate
609 survival. *Geophysical Research Letters - GEOPHYS RES LETT*, 30, 37–1.
610 <https://doi.org/10.1029/2002GL016326>

611 Renette, C. (2024). Dataset for: "Multitemporal UAV LiDAR detects seasonal heave and subsidence on
612 palsas" (Renette et al., 2024) V1.0, Zenodo [data set], 10.5281/zenodo.10497094

613 Romanovsky, V. E., & Osterkamp, T. E. (1995). Interannual variations of the thermal regime of the active
614 layer and near-surface permafrost in northern Alaska. *Permafrost and Periglacial Processes*,
615 6(4), 313–335. <https://doi.org/10.1002/ppp.3430060404>

616 Roulet, N. T. (1991). Surface Level and Water Table Fluctuations in a Subarctic Fen. *Arctic and Alpine*
617 *Research*, 23(3), 303–310. <https://doi.org/10.2307/1551608>

618 Seppälä, M. (1986). The Origin of Palsas. *Geografiska Annaler: Series A, Physical Geography*, 68(3),
619 141–147. <https://doi.org/10.1080/04353676.1986.11880167>

620 Siewert, M. B., & Olofsson, J. (2020). Scale-dependency of Arctic ecosystem properties revealed by UAV.
621 *Environmental Research Letters*, 15(9), 094030. <https://doi.org/10.1088/1748-9326/aba20b>

622 Sjöberg, Y., Coon, E., K. Sannel, A. B., Pannetier, R., Harp, D., Frampton, A., Painter, S. L., & Lyon, S.
623 W. (2016). Thermal effects of groundwater flow through subarctic fens: A case study based on
624 field observations and numerical modeling. *Water Resources Research*, 52(3), 1591–1606.
625 <https://doi.org/10.1002/2015WR017571>

626 Sjögersten, S., Ledger, M., Siewert, M., De la Barreda-Bautista, B., Sowter, A., Gee, D., Foody, G., &
627 Boyd, D. (2023). Optical and radar Earth observation data for upscaling methane emissions
628 linked to permafrost degradation in sub-Arctic peatlands in northern Sweden. *Biogeosciences*, 20,
629 4221–4239. <https://doi.org/10.5194/bg-20-4221-2023>

630 Smith, S. L., O'Neill, H. B., Isaksen, K., Noetzli, J., & Romanovsky, V. E. (2022). The changing thermal
631 state of permafrost. *Nature Reviews Earth & Environment*, 3(1), Article 1.
632 <https://doi.org/10.1038/s43017-021-00240-1>

633 Swindles, G. T., Morris, P. J., Mullan, D., Watson, E. J., Turner, T. E., Roland, T. P., Amesbury, M. J.,
634 Kokfelt, U., Schoning, K., Pratte, S., Gallego-Sala, A., Charman, D. J., Sanderson, N., Garneau,
635 M., Carrivick, J. L., Woulds, C., Holden, J., Parry, L., & Galloway, J. M. (2015). The long-term fate
636 of permafrost peatlands under rapid climate warming. *Scientific Reports*, 5(1), Article 1.
637 <https://doi.org/10.1038/srep17951>

638 Taylor, J. R. (1997). Introduction to Error Analysis, the Study of Uncertainties in Physical Measurements
639 (2nd ed.). *University Science Books*, ISBN 093570275X.

640 Valman, S., Siewert, M. B., Boyd, D., Ledger, M., Gee, D., de la Barreda-Bautista, B., Sowter, A., &
641 Sjögersten, S. (2024). InSAR-measured permafrost degradation of palsa peatlands in northern
642 Sweden. *The Cryosphere*, 18(4), 1773–1790. <https://doi.org/10.5194/tc-18-1773-2024>

643 Verdonen, M., Störmer, A., Lotsari, E., Korpelainen, P., Burkhard, B., Colpaert, A., & Kumpula, T. (2023).
644 Permafrost degradation at two monitored palsa mires in north-west Finland. *The Cryosphere*,
645 17(5), 1803–1819. <https://doi.org/10.5194/tc-17-1803-2023>

646 Voigt, C., Marushchak, M. E., Mastepanov, M., Lamprecht, R. E., Christensen, T. R., Dorodnikov, M.,
647 Jackowicz-Korczyński, M., Lindgren, A., Lohila, A., Nykänen, H., Oinonen, M., Oksanen, T.,
648 Palonen, V., Treat, C. C., Martikainen, P. J., & Biasi, C. (2019). Ecosystem carbon response of
649 an Arctic peatland to simulated permafrost thaw. *Global Change Biology*, 25(5), 1746–1764.
650 <https://doi.org/10.1111/gcb.14574>

651 Walvoord, M. A., & Kurylyk, B. L. (2016). Hydraulic impacts of permafrost thawing and implications for
652 groundwater fluxes in the Arctic. *Water Resources Research*, 52(2), 1236–1255.
653 <https://doi.org/10.1002/2015WR018299>

654 Yanagiya, K., Furuya, M., Danilov, P., & Iwahana, G. (2023). Transient Freeze-Thaw Deformation
655 Responses to the 2018 and 2019 Fires Near Batagaika Megaslump, Northeast Siberia. *Journal of*
656 *Geophysical Research: Earth Surface*, 128. <https://doi.org/10.1029/2022JF006817>

657 Zhang, T. (2005). Influence of the seasonal snow cover on the ground thermal regime: An overview.
658 *Reviews of Geophysics - REV GEOPHYS*, 43. <https://doi.org/10.1029/2004RG000157>

659 Zhang, W., Qi, J., Wan, P., Wang, H., Xie, D., Wang, X., & Yan, G. (2016). An Easy-to-Use Airborne
660 LiDAR Data Filtering Method Based on Cloth Simulation. *Remote Sensing*, 8(6), Article 6.
661 <https://doi.org/10.3390/rs8060501>

662 Zwieback, S., & Meyer, F. J. (2021). Top-of-permafrost ground ice indicated by remotely sensed late-
663 season subsidence. *The Cryosphere*, 15(4), 2041–2055. <https://doi.org/10.5194/tc-15-2041-2021>

664

665